

A New Level Set Numerical Wave Tank with Improved Density Interpolation for Complex Wave Hydrodynamics

Hans Bihs*, Arun Kamath, Mayilvahanan Alagan Chella, Ankit Aggarwal, Øivind A. Arntsen
Department of Civil and Environmental Engineering, Norwegian University of Science and
Technology (NTNU), 7491 Trondheim, Norway

Computers and Fluids, 2016, **140**, pp. 191-208.
DOI: <http://dx.doi.org/10.1016/j.compfluid.2016.09.012>

Abstract

A new three-dimensional numerical wave tank is developed for the calculation of wave propagation and wave hydrodynamics by solving the incompressible Navier-Stokes equations. The free surface is modeled with the level set method based on a two-phase flow approximation, allowing for the simulation of complex phenomena such as wave breaking. The convection terms of the momentum and the level set equations are discretized with the finite difference version of the fifth-order WENO scheme. Time stepping is handled with the third-order TVD Runge-Kutta scheme. The equations are solved on a staggered Cartesian grid, with a ghost cell immersed boundary method for the treatment of irregular cells. Waves are generated at the inlet and dissipated at the numerical beach with the relaxation method. The choice of the numerical grid and discretization methods leads to excellent accuracy and stability for the challenging calculation of free surface waves. The performance of the numerical model is validated and verified through several benchmark cases: solitary wave interaction with a rectangular abutment, wave forces on a vertical cylinder, wave propagation over a submerged bar and plunging breaking waves on a sloping bed.

Keywords: numerical wave tank, wave propagation, wave hydrodynamics, breaking waves, wave forces

1 Introduction

The choice of model for the wave propagation and transformation calculation depends on the required detail and resolution. For large scale wave modeling, such as the wave transformation from deep to shallow waters, spectral wave models such as SWAN [5] are used. This type of model solves the wave action or energy balance equation, which describes the wave

*Corresponding author, hans.bihs@ntnu.no

Postprint, published in *Computers and Fluids*, doi: <http://dx.doi.org/10.1016/j.compfluid.2016.09.012>

spectrum evolution in space and time. The modeled waves are consequently phase averaged. Spectral wave models have been successfully applied to a variety of coastal problems [39][52]. For a range of water wave engineering problems, more detail is required concerning the wave transformation process, including phase information. Phase resolving models based on the Boussinesq equations [30][35] or the parabolic mild-slope equation [27] have the capability to accurately model wave reflection and diffraction. The mild-slope approach is based on the assumption of a mildly sloping sea bottom and linear monochromatic waves. Standard Boussinesq-type models are based on the shallow water equations for non-dispersive linear wave propagation. Extended versions of the Boussinesq equations make it possible to predict wave propagation and transformation from deep to shallow water with the help of improved dispersive terms [29]. When it comes to engineering applications, such as wave propagation in nearshore and harbor areas, Boussinesq-type models are often the preferred engineering solution.

Yet another approach to wave modeling is the class of Fully Nonlinear Potential Flow Models (FNPF), which neglect the effects of viscosity and rotational flow. Here, the Laplace equation for the flow potential is solved with the Boundary Element Method. A Finite Element Method (FEM) and a Mixed Finite Element (MFEM) based method based on the potential theory was presented [51]. A Mixed Eulerian-Lagrangian (MEL) method was shown [18] and could simulate wave transformation up to the point of wave breaking. A higher-order spectral method for the simulation of nonlinear waves was presented [10] with application to the evolution of a wave packet. The potential flow models work well for a range of problems, such as wave propagation in deep water [11] or wave shoaling in shallow water [16]. All mentioned wave models have in common, that they give up a certain level of detail for the benefit of reduced computational cost. For a lot of water wave engineering problems, this is a perfectly reasonable choice.

On the other hand there are complex cases, such as breaking wave kinematics or flow around slender structures, where a more detailed solution is required in order to capture the relevant flow physics. The solution of the three-dimensional Navier-Stokes equations resolves even more detail of the flow processes. Here, the approach is to solve for the basic underlying flow variables, such as the velocities, the pressure and turbulence. Together with the appropriate algorithms for the interface capturing, the free surface and resulting water wave dynamics can be calculated based on the three-dimensional flow field. In order to avoid the unphysical damping of propagating waves due to numerical diffusion, the usage of the Navier-Stokes equations imposes strict criteria for the mesh resolution, the time step size as well as the general accuracy of the numerical algorithm. There have been several studies where Navier-Stokes solvers in conjunction with interface capturing schemes have been used to calculate complex free surface flows such as [47], [55], [9] and [6]. In the current study the focus is exclusively on the demanding problem of wave propagation and wave hydrodynamics. Some successful efforts have been made to use a CFD program as a numerical wave tank, e.g. [24] or [20]. In these methods, the CFD model calculates the free surface with a Volume-of-Fluid (VOF) algorithm, based on convection of the fraction function and interface-compression [48]. The governing equations are solved on a collocated unstructured grid with second-order accuracy for the spatial and temporal discretization. In both cases [24] [20], algorithms for the wave generation and absorption were implemented, resulting in a three-dimensional numerical wave tank. The models were applied to typical laboratory experiments for wave propagation, showing that with today's efficient numerical models and computational resources, very complex

wave propagation simulations can be performed [37][22][40].

In this work, the open-source model REEF3D [1] is presented with alternative approaches for the underlying grid architecture, discretization of the governing equations and treatment of the complex free surface. As mentioned above, numerical accuracy and stability are essential for the good performance of a Navier-Stokes equations based numerical wave tank. Under this premise, the appropriate numerical algorithms were chosen for REEF3D. The level set method is used for the capturing of the free water surface [36]. It has been used for describing two-phase flow with water-air interfaces in several studies [55][53][9]. Geometric Volume-of-Fluid (VOF) algorithms have shown to give better mass conservation properties than the level set method [47]. On the other hand, high-order temporal and spatial discretization can be used for the level set function, which avoid unphysical damping of the propagating water waves. Further, the equations of fluid motion are solved on a staggered grid, ensuring tight velocity-pressure coupling. The Cartesian grid makes it possible to employ the fifth-order Weighted Essentially Non-Oscillatory (WENO) scheme [26] for convection discretization, which delivers accurate and stable solutions. Also for the discretization in time, a high-order method is selected with the third-order total variation diminishing (TVD) Runge-Kutta scheme [41]. As a result, wave propagation and transformation can be calculated throughout the wave steepness range up to the point of wave breaking and beyond, with no artificially high air velocities impacting the quality of the free surface. In Section 2, the numerical methods for the solution of the Navier-Stokes equations are discussed. In Section 3, the free surface treatment and the details of the numerical wave tank implementation are presented. The numerical results of several benchmark wave applications are given in Section 4, before the conclusion in Section 5.

2 Numerical Model

2.1 Governing Equations

The incompressible fluid flow is described by the three-dimensional Reynolds-Averaged Navier-Stokes equations (RANS), which are solved together with the continuity equation for prescribing momentum and mass conservation:

$$\frac{\partial u_i}{\partial x_i} = 0 \quad (1)$$

$$\frac{\partial u_i}{\partial t} + u_j \frac{\partial u_i}{\partial x_j} = -\frac{1}{\rho} \frac{\partial p}{\partial x_i} + \frac{\partial}{\partial x_j} \left[(\nu + \nu_t) \left(\frac{\partial u_i}{\partial x_j} + \frac{\partial u_j}{\partial x_i} \right) \right] + g_i \quad (2)$$

where u is the velocity averaged over time t , ρ is the fluid density, p is the pressure, ν is the kinematic viscosity, ν_t is the eddy viscosity and g the acceleration due to gravity.

The eddy viscosity ν_t in the RANS equations is determined through the two-equation k - ω model [50], with the equations for the turbulent kinetic energy k and the specific turbulent dissipation ω as follows:

$$\frac{\partial k}{\partial t} + u_j \frac{\partial k}{\partial x_j} = \frac{\partial}{\partial x_j} \left[\left(\nu + \frac{\nu_t}{\sigma_k} \right) \frac{\partial k}{\partial x_j} \right] + P_k - \beta_k k \omega \quad (3)$$

$$\frac{\partial \omega}{\partial t} + u_j \frac{\partial \omega}{\partial x_j} = \frac{\partial}{\partial x_j} \left[\left(\nu + \frac{\nu_t}{\sigma_\omega} \right) \frac{\partial \omega}{\partial x_j} \right] + \frac{\omega}{k} \alpha P_k - \beta \omega^2 \quad (4)$$

where P_k is the turbulent production rate, the coefficients have the values $\alpha = \frac{5}{9}$, $\beta_k = \frac{9}{100}$, $\beta = \frac{3}{40}$, $\sigma_k = 2$ and $\sigma_\omega = 2$. In the oscillatory flow motion that characterizes the wave flow field, the mean rate of strain \mathbf{S} can be large. In order to avoid overproduction of turbulence in highly strained flow outside the boundary layer, the turbulent eddy viscosity ν_t is bounded through the following limited formulation [12]:

$$\nu_t = \min \left(\frac{k}{\omega}, \sqrt{\frac{2}{3}} \frac{k}{|\mathbf{S}|} \right) \quad (5)$$

The turbulent length scales in the water are reduced in the proximity of the free surface, leading to increased turbulent dissipation in this region. Also, the turbulent fluctuations normal to the free surface are damped, as their intensity is redistributed to the ones parallel to the interface. When modeling two-phase flow, this behavior is not directly captured by a RANS turbulence model. As \mathbf{S} can be large especially in the vicinity of the interface between water and air, standard RANS turbulence closure will incorrectly predict maximum turbulence intensity at the free surface. Through the implementation of an additional turbulence damping scheme, a more realistic representation of the free surface effect on the turbulence can be achieved [33]. The specific turbulent dissipation at the free surface is defined as:

$$\omega_s = \frac{c_\mu^{-\frac{1}{4}}}{\kappa} k^{\frac{1}{2}} \cdot \left(\frac{1}{y'} + \frac{1}{y^*} \right) \quad (6)$$

where $c_\mu = 0.07$ and $\kappa = 0.4$. The variable y' is the virtual origin of the turbulent length scale, and was empirically found to be 0.07 times the mean water depth [23]. Including the distance y^* from the nearest wall gives a smooth transition from the free surface value to the wall boundary value of ω . The term for the specific turbulent dissipation ω_s is activated around the interface of thickness ϵ by multiplying it with the Dirac delta function $\delta(\phi)$:

$$\delta(\phi) = \begin{cases} \frac{1}{2\epsilon} \left(1 + \cos \left(\frac{\pi\phi}{\epsilon} \right) \right) & \text{if } |\phi| < \epsilon \\ 0 & \text{else} \end{cases} \quad (7)$$

The pressure gradient term in the RANS equations is modeled with Chorin's projection method [8] for incompressible flow on a staggered grid. The staggered grid configuration ensures a tight velocity-pressure coupling. The pressure gradient is removed from the momentum equations. The updated velocity after each Euler step of the Runge-Kutta time discretization is the intermediate velocity u_i^* . Then the Poisson equation for the pressure is formed by calculating the divergence of the intermediate velocity field:

$$-\frac{\partial}{\partial x_i} \left(\frac{1}{\rho(\phi^n)} \frac{\partial p}{\partial x_i} \right) = -\frac{1}{\Delta t} \frac{\partial u_i^*}{\partial x_i} \quad (8)$$

The Poisson equation is solved using the fully parallelized Jacobi-preconditioned BiCGStab algorithm [45]. The pressure is then used to correct the intermediate velocity field, resulting

in the divergence free velocity at the new time step:

$$u_i^{n+1} = u_i^* - \frac{\Delta t}{\rho(\phi_i^n)} \frac{\partial p}{\partial x_i} \quad (9)$$

2.2 Discretization of the Convective Terms

The convective terms of the RANS equations are discretized with the fifth-order WENO scheme [26] in the conservative finite-difference framework. The convection term of the velocity component in x -direction is approximated as follows:

$$u_i \frac{\partial u_i}{\partial x_i} \approx \frac{1}{\Delta x} (\tilde{u}_{i+1/2} u_{i+1/2} - \tilde{u}_{i-1/2} u_{i-1/2}) \quad (10)$$

Here \tilde{u} is the convection velocity, which is obtained at the cell faces through simple interpolation. For the cell face $i + 1/2$, $u_{i+1/2}$ is reconstructed with the WENO procedure:

$$U_{i+1/2}^\pm = \omega_1^\pm U_{i+1/2}^{1\pm} + \omega_2^\pm U_{i+1/2}^{2\pm} + \omega_3^\pm U_{i+1/2}^{3\pm} \quad (11)$$

The \pm sign indicates the upwind direction. U^1 , U^2 and U^3 represent the three possible ENO stencils. For upwind direction in the positive i -direction, they are:

$$\begin{aligned} U_{i+1/2}^{1-} &= \frac{1}{3}u_{i-2} - \frac{7}{6}u_{i-1} + \frac{11}{6}u_i, \\ U_{i+1/2}^{2-} &= -\frac{1}{6}u_{i-1} + \frac{5}{6}u_i + \frac{1}{3}u_{i+1}, \\ U_{i+1/2}^{3-} &= \frac{1}{3}u_i + \frac{5}{6}u_{i+1} - \frac{1}{6}u_{i+2} \end{aligned} \quad (12)$$

The nonlinear weights ω_n^\pm are determined for each ENO stencil and calculated based on the smoothness indicators IS [26]. Large smoothness indicators indicate a non-smooth solution in the particular ENO stencil. Accordingly, the non linear weights ω_n for this stencil will be small. The WENO scheme favors stencils with a smooth solution and assigns them the largest weights ω_n . As a result the scheme can handle large gradients right up to the shock very accurately. In the worst-case situation, the WENO scheme will achieve a third-order of accuracy. In the areas where the solution is smooth, it will deliver fifth-order accurate results. In comparison to high resolution schemes such as MUSCL [46] or TVD [19] schemes, the WENO scheme does not smear out the solution. Instead, it maintains the sharpness of the extrema. The conservative WENO scheme is used to treat the convective terms for the velocities u_i , while the Hamilton-Jacobi version is used for the variables of the free surface and turbulence algorithms.

2.3 Time Advancement Scheme

For the time treatment of the momentum and the level set equations, a third-order accurate TVD Runge-Kutta scheme is employed, consisting of three Euler steps [41].

$$\begin{aligned}
 \phi^{(1)} &= \phi^n + \Delta t L(\phi^n) \\
 \phi^{(2)} &= \frac{3}{4}\phi^n + \frac{1}{4}\phi^{(1)} + \frac{1}{4}\Delta t L(\phi^{(1)}) \\
 \phi^{n+1} &= \frac{1}{3}\phi^n + \frac{2}{3}\phi^{(2)} + \frac{2}{3}\Delta t L(\phi^{(2)})
 \end{aligned}
 \tag{13}$$

This scheme provides a high-order of temporal accuracy, and for CFL numbers below 1 it shows very good numerical stability through its TVD properties. Adaptive time stepping is used in order to control the CFL number and takes the influence from velocity, diffusion and the source term S , such as for example gravity, into account [15]. The time step size Δt is determined as follows:

$$\Delta t \leq 2 \left(\left(\frac{|u|_{max}}{dx} + D \right) + \sqrt{\left(\frac{|u|_{max}}{dx} + D \right)^2 + \frac{4|S_{max}|}{dx}} \right)^{-1}
 \tag{14}$$

with the contribution from the diffusion term D :

$$D = \max(\nu + \nu_t) \cdot \left(\frac{2}{(dx)^2} + \frac{2}{(dy)^2} + \frac{2}{(dz)^2} \right)
 \tag{15}$$

For a RANS model, where the turbulence magnitude is expressed through the eddy viscosity, the diffusion criterion of the order ν_{max}/dx^2 can become prohibitively restrictive. As a solution, the diffusion part of the RANS equation is treated implicitly in the current numerical model, thus removing it from the CFL criterion. The third-order accurate TVD Runge-Kutta scheme is used for all transport equations in the numerical wave tank with the exception of the turbulence model. A special characteristic of two-equation turbulence models is that they are mostly source term driven, namely by the turbulent production and dissipation terms. In comparison to the momentum equation, the convective and diffusive terms play only a minor role. For explicit time discretization of the k and ω equations, the large source terms result in a significantly smaller time step than for the momentum equations due to the CFL criterion. Instead of letting the turbulence model determine the time step, its equations are discretized with a first-order implicit Euler scheme.

2.4 Immersed Boundary

The numerical model uses a Cartesian grid in order to employ high-order discretization schemes. An additional benefit comes from the straightforward implementation of numerical algorithms, as the geometry of the numerical cells is trivial in this case. The challenge of irregular, non-orthogonal solid boundaries is overcome with the implementation of the immersed boundary method. In REEF3D, a ghost cell immersed boundary method (GCIBM) is used [4]. In this method, the solution is analytically continued through the solid boundary

by updating fictitious ghost cells in the solid region by extrapolation. This way, the numerical discretization does not need to account for the boundary conditions explicitly, instead they are enforced implicitly. The algorithm is based on the local directional approach [4], which was implemented in two dimensions. For the current model it has been extended to three dimensions. In the original GCIBM, the fluid values are extrapolated orthogonal to the boundary into the solid [44][32], which can become difficult for sharp corners. In the local directional GCIBM the values from the fluid are extrapolated into the solid along the coordinate directions [4].

In REEF3D, grids can be generated based on geometric primitives, such as boxes, cylinders and wedges. More complex geometries can be read in .STL format and immersed into the Cartesian grid, following the strategy presented in [54]. For natural bathymetries with measured x , y and z coordinates, the solid boundary can be represented by a level set function. Then, the location of the level set function is calculated from the coordinates with either inverse-distance or kriging interpolation.

2.5 Parallelization

The efficient computation of CFD results depends to a large extent on the strategy for the parallelization of the numerical model. In REEF3D, parallelization is achieved through domain decomposition. Here, the simulation domain is split into smaller parts, each of them communicating with their neighbors through ghost cells. Because REEF3D already uses the ghost cell method for the solid boundaries, this approach is straightforward to code and consistent with the treatment of the other domain boundaries. The message passing interface (MPI) is used for the implementation of the ghost cell value exchange. Since a fifth-order WENO scheme is used for the convection discretization of the velocities, the level set function and the variables of the turbulence model, three ghost cell levels are required. For the pressure, only one level of ghost cells is needed. The code is employed on NOTUR’s supercomputer Vilje [34], which is an “SGI Altix 8600” cluster. Vilje consists of 1404 nodes with two 8-core processors on each node, resulting in a total of 22464 cores.

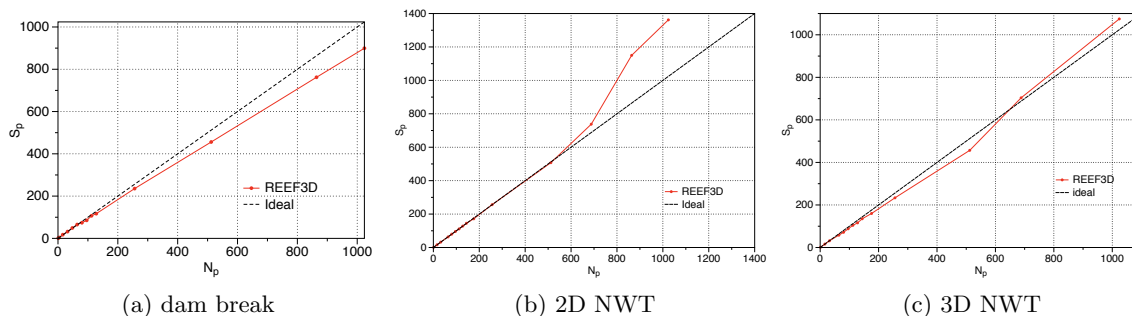


Figure 1: Parallel scaling test for dam break, 2D wave tank and 3D wave tank

In order to investigate the parallel efficiency of REEF3D, a 3D dam break test, a 2D numerical wave tank (NWT) and a 3D NWT were simulated for 100 iterations. For the 3D dam break, a domain of size ($L_x \times L_y \times L_z = 1 \text{ m} \times 1 \text{ m} \times 1 \text{ m}$) is used with a grid size $dx = 0.005 \text{ m}$ with a total of 8 million cells. A water column 0.8 m high and 0.3 m long

N_p	dam break		2D NWT		3D NWT	
	CPU time (s)	S_p	CPU time (s)	S_p	CPU time (s)	S_p
1	998.4	1	7968	1	950	1
4	249.6	4	1992	4	237.5	4
16	57.2	17.45	498	16	59.5	15.97
32	31.2	32	249	32	30	31.67
48	20.3	49.18	165.3	48.2	21.1	45.02
64	15.3	65.25	126	63.24	16.4	57.93
80	13.5	73.96	100	79.68	13.3	71.43
96	11.7	85.34	83.2	95.77	10.8	87.96
112	9.35	106.78	71.7	111.13	9.12	104.17
128	8.54	116.91	62.3	127.9	8.20	115.85
256	4.24	235.47	31.1	256.21	4.07	233.42
512	2.19	455.89	15.7	507.52	2.08	456.73
864	1.31	762.14	6.93	1149.8	1.13	840.71
1024	1.11	899.46	5.85	1362.1	0.844	1074.7

Table 1: CPU times and Speedup (S_p) for each test case

collapses along the 1 m width of the domain. For the 2D NWT test, a rectangular wave tank with the domain size ($L_x \times L_z = 62 \text{ m} \times 4 \text{ m}$) and a mesh size of $dx = 0.005 \text{ m}$ has a total of 9.92 million cells. For the 3D NWT test, a wave tank with the domain size of ($L_x \times L_y \times L_z = 250 \text{ m} \times 5 \text{ m} \times 8 \text{ m}$), a mesh size of $dx = 0.1 \text{ m}$ and a total of 10 million cells is used. As seen from Fig. (1a), the parallel speedup (S_p) for the 3D dam break follows the ideal scaling up to 80 processors. Further, the speedup (S_p) is slightly reduced and the speedup for 1024 processors is 899.5. For the 2D NWT in Fig. (1b), the ideal scaling is followed up to 688 processors. After that, the speedup is even further improved. For the 3D NWT, the parallel speedup of the model shown in Fig.(1c) is close to the ideal situation up to the maximum number of tested processor cores. A difference is seen between the speedup in the different test cases. This can be attributed to the geometry of the numerical domain used in the test cases. In the case of the 3D dam break, the geometry is uniformly spread in the three directions with a 1:1:1 aspect ratio. Then, the decomposition is homogenous for all the processors and the number of ghost cells is the same in all three coordinate directions. The slight reduction in speedup seen with the increase in the number of processors is due to the overhead from parallel communication. In the case of the NWT test in 2D, the spatial domain along the x - direction is much larger than the extent along the y - and z - directions. In these cases, as the number of processors are increased, the decomposition of the spatial domain results in the smaller partitions. Due to the skewed aspect ratio, the length of the domain along the x - direction is smaller compared to the y - direction. As the number of processors is further increased, the gain in computational speed outweighs the parallel communication overhead and a near-ideal speedup is obtained. The 3D NWT test follows a similar trend. A summary of the CPU times taken and the speedup calculated for each test case is listed in Table (1).

3 Numerical Wave Tank

3.1 Free Surface Capturing

The location of the free water surface is represented implicitly by the zero level set of the smooth signed distance function $\phi(\vec{x}, t)$ [36]. The level set function gives the closest distance to the interface Γ and the two phases are distinguished by the change of the sign. This results in the following properties:

$$\phi(\vec{x}, t) \begin{cases} > 0 \text{ if } \vec{x} \in \text{phase 1} \\ = 0 \text{ if } \vec{x} \in \Gamma \\ < 0 \text{ if } \vec{x} \in \text{phase 2} \end{cases} \quad (16)$$

In addition, the Eikonal equation $|\nabla\phi| = 1$ is valid. When the interface Γ is moved under an externally generated velocity field \vec{u} , a convection equation for the level set function is obtained:

$$\frac{\partial\phi}{\partial t} + u_j \frac{\partial\phi}{\partial x_j} = 0 \quad (17)$$

The convection term in Eq. (17) is solved with the Hamilton-Jacobi version of the WENO scheme [25]. For time stepping, the third-order TVD Runge-Kutta scheme is used [41]. When the interface evolves, the level set function loses its signed distance property. In order to maintain this property and to ensure mass conservation, the level set function is reinitialized after each time step. In the present paper, a PDE based reinitialization equation is solved [42]:

$$\frac{\partial\phi}{\partial t} + S(\phi) \left(\left| \frac{\partial\phi}{\partial x_j} \right| - 1 \right) = 0 \quad (18)$$

where $S(\phi)$ is the smoothed sign function [38].

3.2 Density Location

With the level set function in place, the material properties of the two phases can be defined for the whole simulation domain. On a staggered grid, the cell face density is required for the calculation of the Poisson equation for the pressure in Eq. (8) and the correction of the velocity with the pressure gradient in Eq. (9). In previous level set based numerical models with staggered grids [47], [6], the density is usually determined at the cell centers with the smoothed Heaviside function in a first step:

$$\rho_i = \rho_1 H(\phi_i) + \rho_2 (1 - H(\phi_i)), \quad (19)$$

with ρ_1 and ρ_2 representing the densities of the two fluids and the Heaviside function

defined as:

$$H(\phi_i) = \begin{cases} 0 & \text{if } \phi_i < -\epsilon \\ \frac{1}{2} \left(1 + \frac{\phi_i}{\epsilon} + \frac{1}{\pi} \sin\left(\frac{\pi\phi_i}{\epsilon}\right) \right) & \text{if } |\phi_i| < \epsilon \\ 1 & \text{if } \phi_i > \epsilon \end{cases} \quad (20)$$

Typically the thickness of the smoothed out interface is chosen to be $\epsilon = 1.6dx$ on both sides of the interface. In a second step, the density at the cell faces is evaluated through simple averaging of the density at the two neighboring cell centers [9]:

$$\rho_{i+\frac{1}{2}} = \frac{1}{2} (\rho_i + \rho_{i+1}) \quad (21)$$

In another example [53], the cell face density is calculated through a linear interpolation based on the location of the interface in the second step. In the current numerical model for the calculation of propagating waves, it was observed that this two-step strategy for the cell face density evaluation leads to small scale oscillations of the free surface. For other types of free-surface flows, such as open-channel flow, this phenomenon could not be reproduced. For the simulation of waves, the oscillations are more pronounced for lower steepness waves. In general, the problem occurs when the free surface is mildly sloped with respect to the orientation of the gridlines in the presence of a vertical velocity component, as is the case for waves.

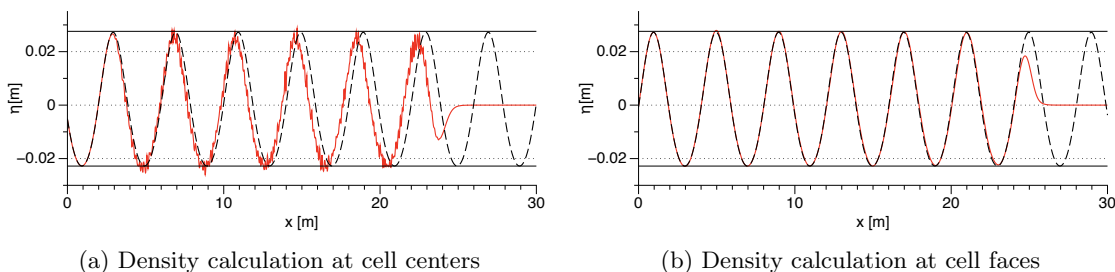


Figure 2: Influence of cell face density calculation on the free surface for periodic waves with wave length $L = 4$ m, wave height $H = 0.05$ m and still water level $d = 0.5$ m in a 30 m long wave flume with $dx = 0.01$ m after 90 s. The black dashed line shows the wave theory, the black solid line the theoretical wave envelope and the red line the numerical model.

In order to illustrate the effect, 2nd-order Stokes waves with a wavelength $L = 4$ m and a wave height $H = 0.05$ m are generated in a 30 m long and 1 m high 2D wave flume with a water depth $d = 0.5$ m on a mesh with $dx = 0.01$ m. Fig. (2a) shows the computed wave surface elevation after 90 s. Comparing it with the theoretical wave profile along the wave flume, the free surface oscillations and a phase shift become visible. The relatively long simulation time of 90 s is chosen, so that the oscillations are fully developed. Even though the quality of the numerical results is clearly degraded, the numerical solution remains stable throughout the simulation with neither excess velocities nor pressure values occurring. As a remedy for the free surface oscillations, the density at the cell faces is calculated in a modified manner. Using

a single step, the density at the cell face is calculated with the smoothed Heaviside function right away:

$$\rho_{i+\frac{1}{2}} = \rho_1 H\left(\phi_{i+\frac{1}{2}}\right) + \rho_2 \left(1 - H\left(\phi_{i+\frac{1}{2}}\right)\right), \quad (22)$$

The level set function at the cell face is calculated through averaging:

$$\phi_{i+\frac{1}{2}} = \frac{1}{2}(\phi_i + \phi_{i+1}) \quad (23)$$

As can be seen in Fig. (2b), the resulting free surface is oscillation-free and the numerical solution matches the theoretical wave profile in both amplitude and phase. Similar to the current findings, [49] identified the importance of the density averaging for the quality of the free surface in the context of the VOF method on a staggered grid. Fig. (3) shows the density profile for the cell faces i across the interface, in a case where the interface is normal to the x -direction. Three different situations are considered: the interface located directly on the cell face, between the cell face and the cell center and directly at the cell center. The density calculation at the cell centers is denoted ρ_{center} , and the density calculation at the cell faces ρ_{face} . Compared to the curve for the cell-centered density evaluation ρ_{center} with $\epsilon = 1.6dx$, the density profile is actually less smoothed out across the interface for ρ_{face} with $\epsilon = 1.6dx$, because the second step with the averaging of the densities is missing. In order to account for this, the current method of the cell face density evaluation uses the interface thickness $\epsilon = 2.1dx$. As can be seen from Fig. (3), for ρ_{face} with $\epsilon = 2.1dx$, the width of the density

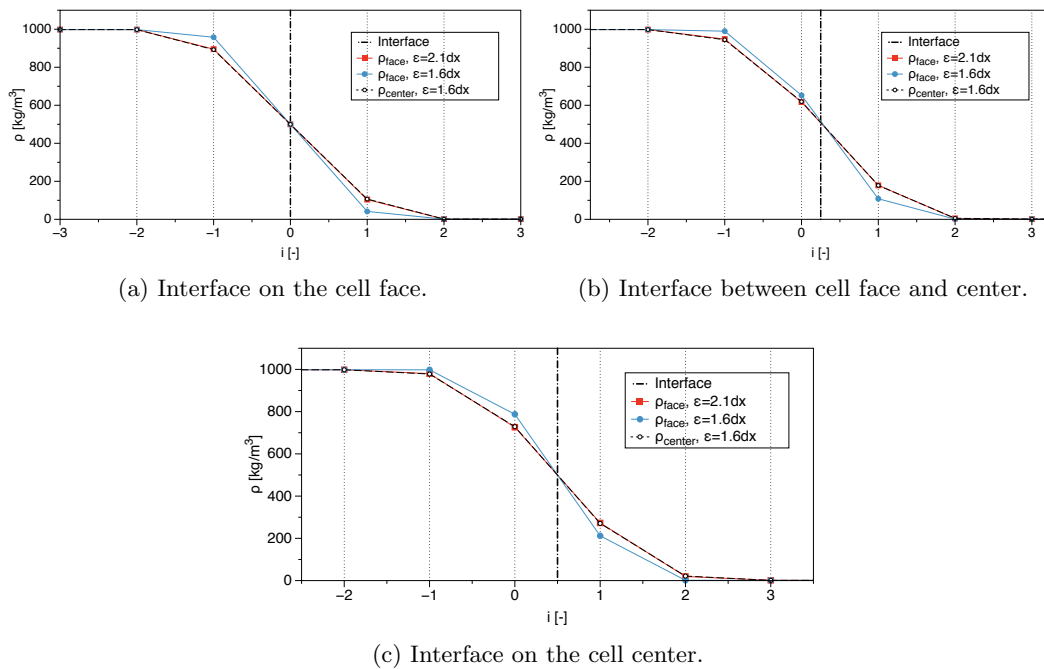


Figure 3: Density profile along the interface at the cell faces for different interface locations and density evaluation schemes. The x -axis i represents the cell centers.

transition area and the magnitude of the density gradient across the interface at the cell faces is the same as for ρ_{center} with $\epsilon = 1.6dx$.

3.3 Wave Generation and Absorption

Typical inlet boundary conditions for free surface flow applications are of Dirichlet type. When generating waves at the inlet, the free surface is in constant motion and the flow direction is changing periodically. As a result, simple Dirichlet type wave generation does not necessarily deliver waves of the highest quality. In REEF3D, waves are generated with the relaxation method, which is presented in [31] and extended for CFD models in [24]. Here, the wave generation takes place in a relaxation zone with a typical size of one wavelength (see Fig. (4)).

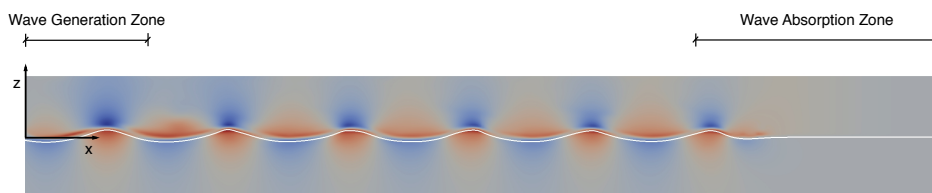


Figure 4: Sketch of the numerical wave tank with wave generation and absorption zones. The contour shows the horizontal velocity component.

The values for the velocities and the free surface are ramped up from the computational values to the values obtained from wave theory (Eq. (24)). The waves are generated without any disturbances occurring at the interface. In addition, reflected waves that travel back towards the inlet are absorbed with this method. At the outlet of a wave flume, the waves need to be dissipated in order to avoid reflections that can negatively impact the numerical results. This can be achieved with the relaxation method. In the numerical beach relaxation zone, the computational values for the horizontal and vertical velocities are smoothly reduced to zero, the free surface to the still water level and the pressure is relaxed to the hydrostatic distribution for the still water level. Thus, the wave energy is effectively absorbed and reflections are prevented.

$$\begin{aligned}
 u(\tilde{x})_{relaxed} &= \Gamma(\tilde{x})u_{analytical} + (1 - \Gamma(\tilde{x}))u_{computational} \\
 w(\tilde{x})_{relaxed} &= \Gamma(\tilde{x})w_{analytical} + (1 - \Gamma(\tilde{x}))w_{computational} \\
 p(\tilde{x})_{relaxed} &= \Gamma(\tilde{x})p_{analytical} + (1 - \Gamma(\tilde{x}))p_{computational} \\
 \phi(\tilde{x})_{relaxed} &= \Gamma(\tilde{x})\phi_{analytical} + (1 - \Gamma(\tilde{x}))\phi_{computational}
 \end{aligned} \tag{24}$$

The relaxation function presented in [24] is used. The wave generation zone has the length of one wavelength, the numerical beach extends over two wavelengths.

$$\Gamma(\tilde{x}) = 1 - \frac{e^{(\tilde{x}^{3.5})} - 1}{e - 1} \text{ for } \tilde{x} \in [0; 1] \tag{25}$$

The coordinate \tilde{x} is scaled to the length of the relaxation zone. Several wave theories are implemented in REEF3D: linear waves, second-order and fifth-order Stokes waves, first-order and fifth-order cnoidal waves, first-order and fifth-order solitary waves and first-order

irregular and focused waves. In case of linear waves for general water depths, the horizontal and vertical velocities u and w and the level set function ϕ for the free surface location are given as:

$$\begin{aligned} u(x, z, t)_{analytical} &= \frac{\pi H \cosh [k(z+d)]}{T \sinh(kd)} \cos\theta \\ w(x, z, t)_{analytical} &= \frac{\pi H \sinh [k(z+d)]}{T \sinh(kd)} \sin\theta \\ \phi(x, z, t)_{analytical} &= \frac{H}{2} \cos\theta - z + d \end{aligned} \tag{26}$$

The wave number k and the wave phase θ are defined as follows:

$$\begin{aligned} k &= \frac{2\pi}{L} \\ \theta &= kx - \omega t \end{aligned} \tag{27}$$

where H is the wave height, L the wavelength, T the wave period, ω the angular wave frequency and z the vertical coordinate with the origin at the still water level d . In the wave generation zone, the pressure is not prescribed in the current numerical model, in order not to over define the boundary conditions. The omission of the pressure prescription in the wave generation zone has not shown a loss in wave quality. At the numerical beach, the pressure is always set to its hydrostatic values based on the still water level d , independent of the wave input.

3.4 Numerical Calculation of Wave Forces

Wave forces can be determined by the numerical model in a straightforward manner. The pressure and the normal component of viscous stress tensor τ are integrated over the surface Ω of the structure. The integration is performed in a discrete manner, by using p and τ for each cell surface of the structure:

$$F = \int_{\Omega} (-\mathbf{n}p + \mathbf{n} \cdot \boldsymbol{\tau}) d\Omega \tag{28}$$

here \mathbf{n} is the unit normal vector to the surface, pointing into the fluid. The Navier-Stokes equations in Eq. (2) are solved including the gravity term. Then the pressure obtained from the projection method includes the hydrostatic part in addition to the dynamic part. Consequently, it is the total force acting on a structure that is determined by Eq. (28).

4 Results

In this section, several numerical results for wave propagation benchmark cases are presented. The numerical model is tested in order show the numerical accuracy and convergence in addition to the overall capabilities of REEF3D.

4.1 Grid and Time Step Convergence Tests

At first the general performance of the numerical model regarding wave propagation is tested in a rectangular wave flume with a two-dimensional setup. Regular waves are generated based on wave theory. Since there is no obstacle or other change in geometry along the wave flume, no wave transformation should take place and the wave should maintain the exact same shape and propagation speed as in the generation zone. As a consequence, the grid and time step convergence tests can be evaluated by comparing the numerical wave profile along the wave flume with the theoretical profile.

For these tests, a wave height of $H = 0.1$ m and a wave length of $L = 2$ m are selected for a still water depth of $d = 0.5$ m in a 20 m long wave flume. The resulting wave is of relatively high steepness ($\xi = H/L = 0.05$), requiring wave generation with fifth-order Stokes theory [13]. This makes it also more challenging for the numerical model to maintain the wave height along the flume without numerical damping. The grid convergence test is performed on four different meshes with $dx = (0.05$ m, 0.025 m, 0.01 m, 0.005 m). For the comparisons in Figs. (5) and (6), the result after 90 s is used. For the grid convergence, the CFL number is kept at 0.1. Fig. (5a) shows the result for $dx = 0.05$ m. Here, the simulated wave troughs and crests are damped out. Also, the wave goes slightly out of phase. For $dx = 0.025$ m (Fig. (5b)) the numerical result improves. Wave crest damping occurs only towards the second half of the wave flume and the wave is in phase. From $dx = 0.01$ m on, the numerical model converges to the theoretical solution (Fig. (5c)). For both $dx = 0.01$ m and $dx = 0.005$ m, no wave crest damping occurs. Only a very slight under prediction of the wave troughs can be observed.

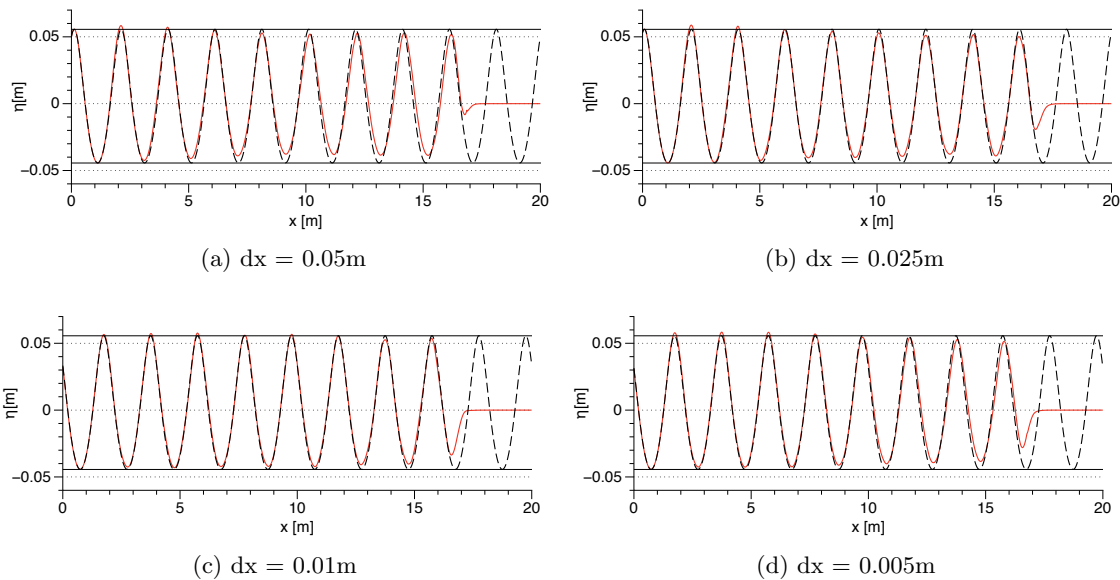


Figure 5: Grid convergence test in a 20 m long 2D wave flume with wave height $H = 0.1$ m, wave length $L = 2$ m and a CFL number of 0.1. The black dashed line shows the wave theory, the black solid line the theoretical wave envelope and the red line the numerical model.

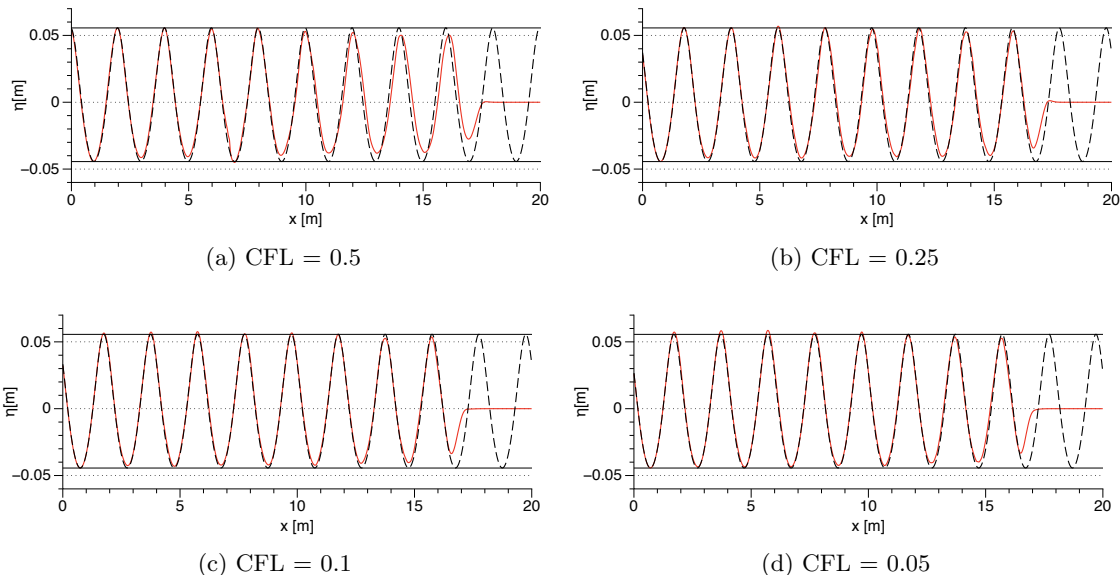


Figure 6: Time step convergence test in a 20 m long 2D wave flume with wave height $H = 0.1$ m, wave length $L = 2$ m and $dx = 0.01$ m. The black dashed line shows the wave theory, the black solid line the theoretical wave envelope and the red line the numerical model.

For the time step convergence test, the same wave conditions as for the grid convergence are used. Since the grid convergence tests showed a converged solution for $dx = 0.01$ m for these wave conditions, this grid size is used here. As presented above, the numerical model employs adaptive time stepping, so instead of testing fixed time step sizes, the CFL numbers 0.5, 0.25, 0.1 and 0.05 are tested. Fig. (6a) with $CFL = 0.5$ shows wave damping and a phase shift towards the end of the flume. For $CFL = 0.25$, the wave is in phase, but minor wave crest damping occurs at the end of the flume. For $CFL = 0.1$ and $CFL = 0.05$, the numerical results look similar (Fig. (6c-d)). No wave crest damping is observed, just a slight under prediction of the the wave trough. The CFL number incorporates information about the mesh width dx , so $CFL = 0.1$ is used for all of the following numerical applications. The mesh width on the other hand is tested for all cases individually.

A convergence study of the numerical wave tank is carried out by calculating the difference along the horizontal and vertical at the peaks and troughs of the generated wave and the theoretically expected waveform. The difference in the location of the peaks along the horizontal provide an estimate of the dispersion error in the numerical wave tank. The amplitude error is obtained from the difference along the vertical. The calculations are carried out for every time step for every 1 m in the working zone of the wave tank. The waves are simulated in a 2D numerical wave tank 25 m long and 1 m high in a water depth $d = 0.5$ m with wave height $H = 0.1$ m and wavelength $L = 2$ m. The simulations are carried out for different grid sizes $dx = 0.1$ m, 0.05 m, 0.025 m, 0.01 m and 0.005 m with $CFL=0.1$ to demonstrate the convergence rate of the model as well.

Fig.(7a) shows the RMS error along the horizontal at the peaks and troughs in the wave tank for $t = 30.0$ s to $t = 90.0$ s. It is seen that the difference between the location of the peaks and the troughs increases along the length of the wave tank. This difference is reduced

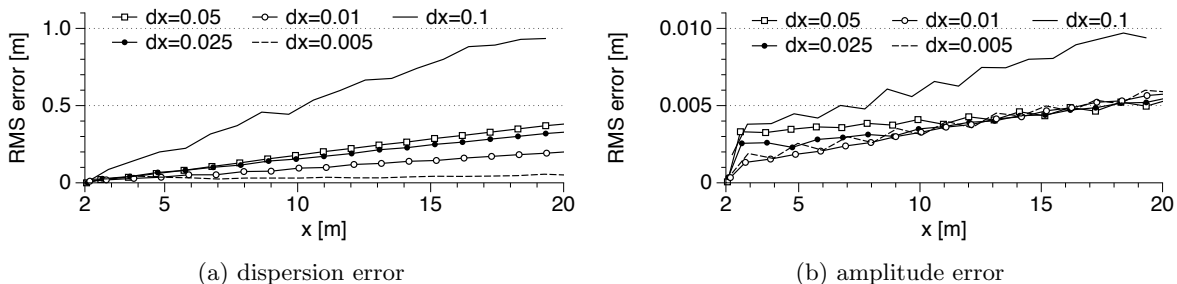


Figure 7: Convergence study for the NWT with dispersion and amplitude RMS errors

as the grid size is reduced and the RMS error at $x = 10.0$ m in the wave tank is 0.44 m for $dx = 0.1$ m and 0.03 m for $dx = 0.005$ m. This means that the difference in the location of the peaks and troughs is 1.5% at $dx = 0.005$ m. From the RMS error along the vertical shown in Fig.(7b) for $t = 30.0$ s to $t = 90.0$ s, it is seen that the overall amplitude error is low in the numerical wave tank. The largest errors are calculated for $dx = 0.1$ m, with an RMS error of 0.0056 m at $x = 10.0$ m. The RMS error for the other grid sizes are almost similar around $x = 10$ m in the wave tank, with an RMS error of 0.00031 for $dx = 0.005$ m, which corresponds to 0.31% of the generated wave height. It seen from the results that the grid size affects wave dispersion more than the wave amplitude. The results for the wave height are converged for even coarser grid sizes in the model. This is a very important aspect as the accurate representation and propagation of the wave height through the wave tank is essential for various wave engineering problems.

4.2 Solitary Wave Interaction with a Rectangular Abutment

In this benchmark case, solitary wave propagation and the interaction with a rectangular abutment is investigated. The simulated results are compared with experimental data [28][21]. In the experiments, a rectangular abutment is placed in a 0.58 m wide wave flume, obstructing the flow over a width of 0.28 m. The side wall and the bottom of the wave flume are made of glass. The still water level is $d = 0.45$ m, a solitary wave with height $H = 0.1$ m is generated with a piston-type wavemaker. A fully reflective wall is placed at the end of the wave flume. In Fig. (8a) the plan view of the setup, including the wave gage locations, can be seen. In the numerical model, the solitary wave is generated from third-order theory [17] in a relaxation zone with the length $l = 8$ m. The numerical domain has the size of ($L_x \times L_y \times L_z = 23.8 \text{ m} \times 0.58 \text{ m} \times 0.9 \text{ m}$). The front face of the abutment is located 14.84 m away from the inlet boundary. This distance is 4 m longer than in the experimental setup, in order to accommodate the wave generation zone. For the grid convergence tests, four different meshes are used with $dx = (0.1 \text{ m}, 0.05 \text{ m}, 0.02 \text{ m}, 0.01 \text{ m})$, resulting in meshes with totals of 0.012 million, 0.1 million, 1.54 million and 12.36 million cells. As can be seen in Fig. (8a), there are nine wave gages placed around the abutment, both in the experimental and the numerical setup and the free surface data comparison is shown in Fig. (9).

All wave gages show two peaks. The first one is for the incoming solitary wave originating from the wavemaker. Then the wave passes the vertical structure and is reflected from the downstream wall. The reflected wave is recorded by the wave gages as the second peak. In

order to perform the grid convergence tests, wave gage 7 is selected for comparison, as it is located downstream of the abutment and the influence of the structure can be seen for the first wave. Remarkably, the first peak is reproduced equally well on all four grids. Only for the reflected wave, the coarsest grid with $dx = 0.1$ m shows a reduced wave peak. The solitary wave is a single crest wave. The higher order WENO discretization of the convection terms ensures that there is no damping of the soliton, making the accurate solution less dependent on the grid size. In Figs. (9a-9i), the results from the fine grid $dx = 0.01$ m are presented.

Gage 1 and 2 in Fig. (9a-b) show the generated solitary wave. The crest of the incident solitary wave is still unaffected by the abutment, maintaining the input wave height of $H = 0.1$ m. Directly after the peak, a slight bump in the wave shape occurs, which is attributed to the partial reflection from the abutment structure. The second peak resulting from the wave reflected by the downstream wall is clearly reduced. Gages 3 and 4 in Fig. (9c-d) show the effect of the channel narrowing. The numerical model calculates increased waves heights of $H = 0.11$ m and $H = 0.13$ m respectively for the incoming wave, slightly higher than the experimental data. For gage 4, the reflected wave is reduced with $H = 0.05$ m as it is shadowed by the vertical structure. Wave gage 5 (Fig. (9e)) is located in the part of the flume that is constricted by the abutment. Here the incoming wave height is reduced. As the flow accelerates and the pressure decreases, a considerable drop in the free surface elevation in the vicinity of the abutment can be observed (Fig. (8b-c)) for the incoming wave. Wave gage 6 (Fig. (9f)) is situated on the downstream side of the abutment. Here the incoming wave height is lower than the reflected wave, mirroring the behavior for gage 4. For gages 7 to 9 (Fig. (8g-i)), the incoming and reflected waves are nearly of the same magnitude. The reason

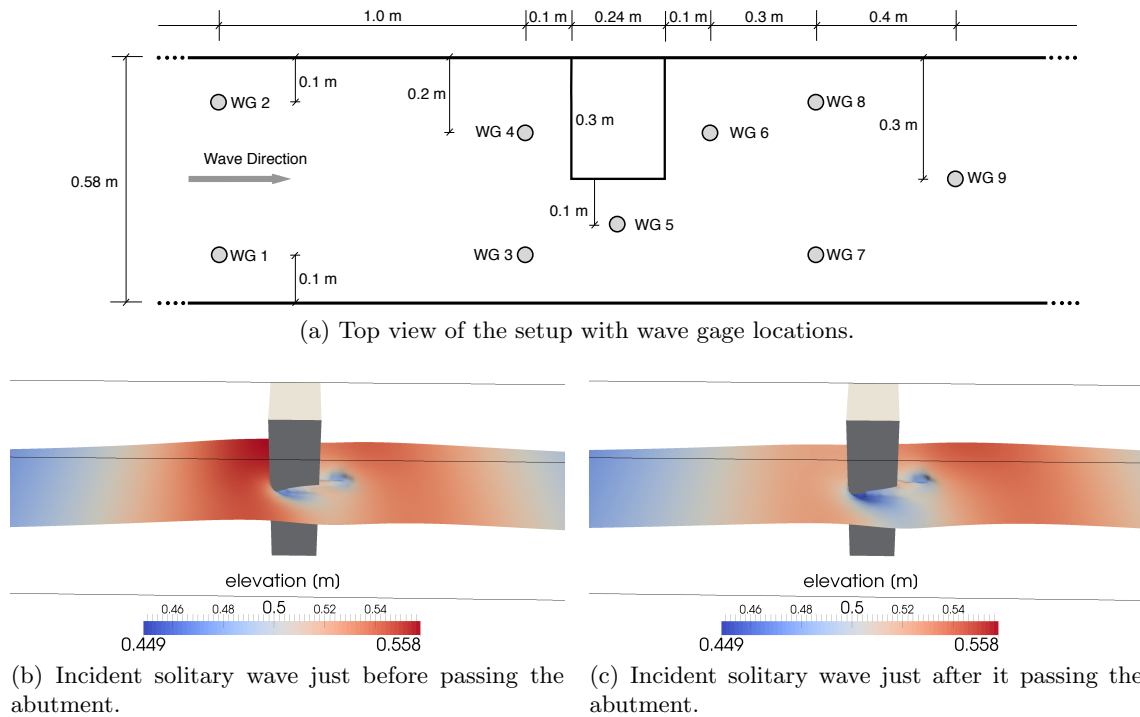


Figure 8: Solitary wave interaction with a rectangular abutment with setup and numerical free surface results.

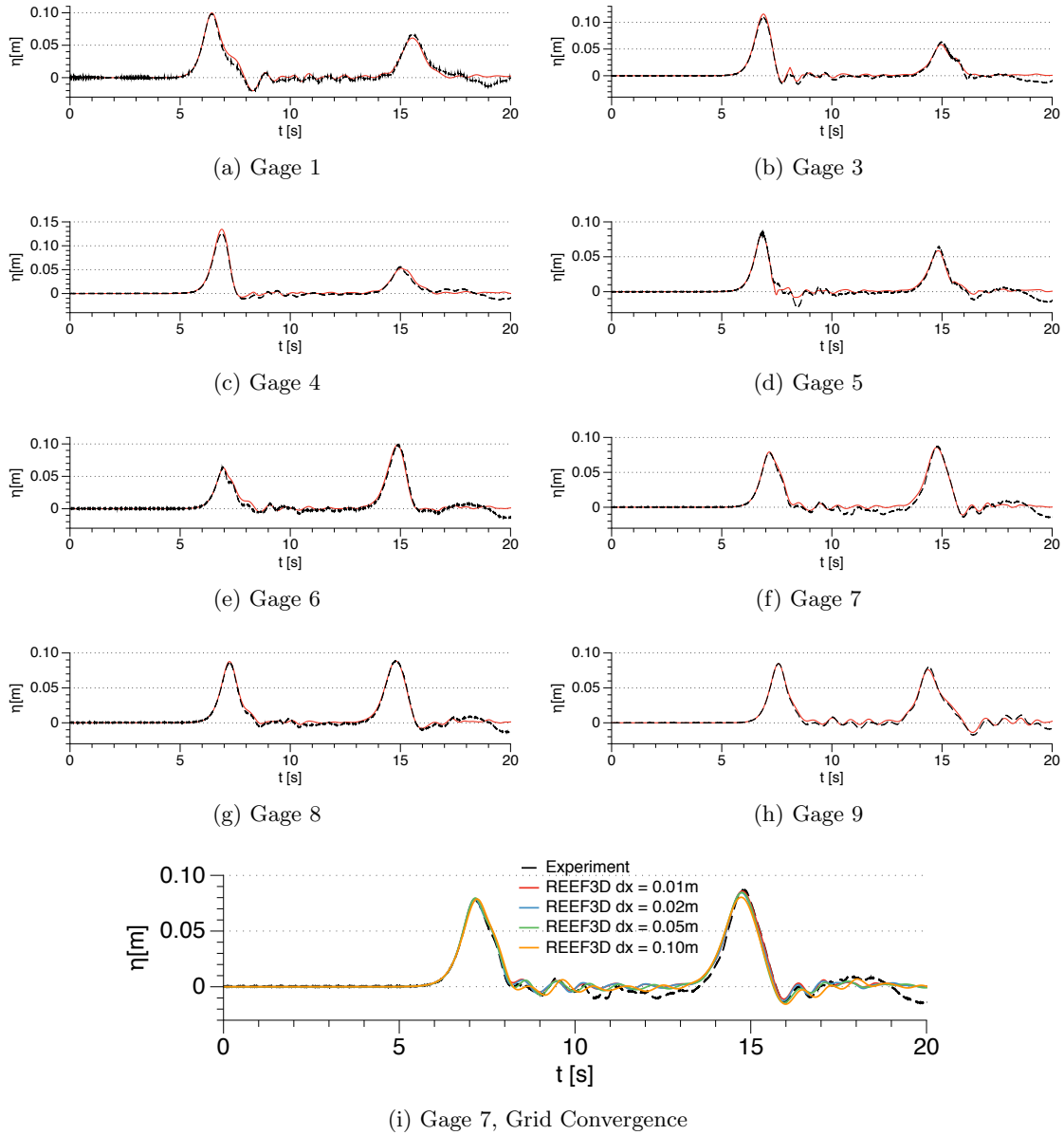


Figure 9: Solitary wave interaction with a vertical structure, black lines are laboratory experiments, red lines are REEF3D.

is that between the incoming wave and the reflection, the wave is not further transformed. In general, the numerical model maintains all the wave peaks and also predicts the wave celerity correctly.

4.3 Wave Interaction with a Vertical Circular Cylinder

Data from the experiments carried out at DHI, Denmark [7] is used for the comparison of the numerical results for wave interaction with a single vertical cylinder. The shallow water basin

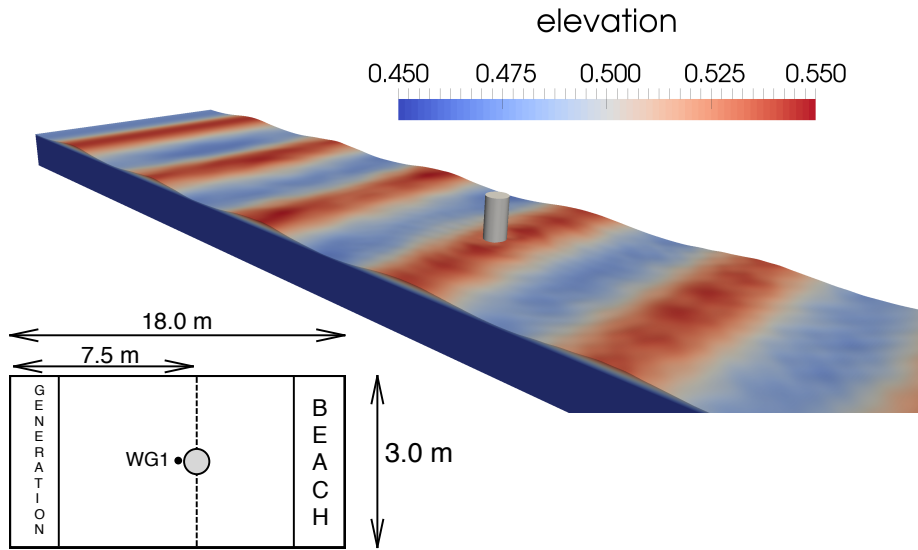


Figure 10: Numerical setup for calculating wave forces on a vertical circular cylinder

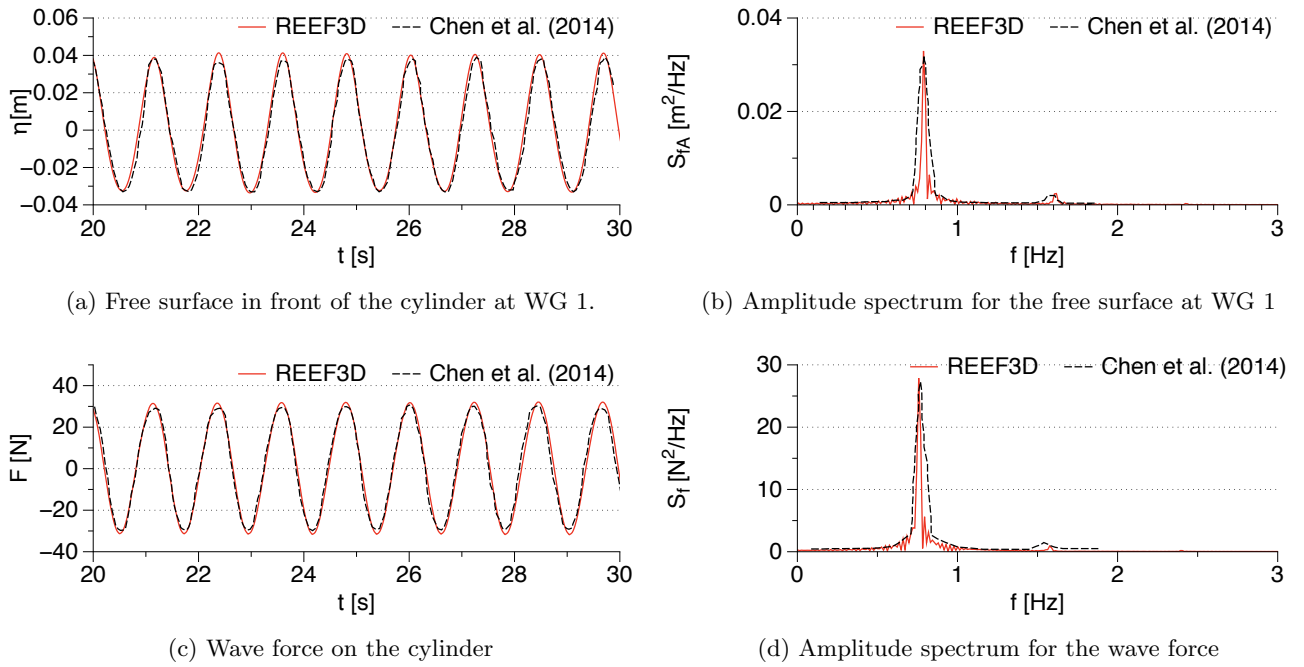


Figure 11: Comparison of experimental [7] and numerical results for wave interaction with a vertical cylinder

used in the experiments is 35 m long, 25 m wide and a water depth of 0.505 m. A cylinder of diameter $D = 0.25$ m is placed at a distance of 7.52 m from the wavemaker. Regular waves of period $T = 1.22$ s and wave height $H = 0.07$ m are generated. The wave force on the

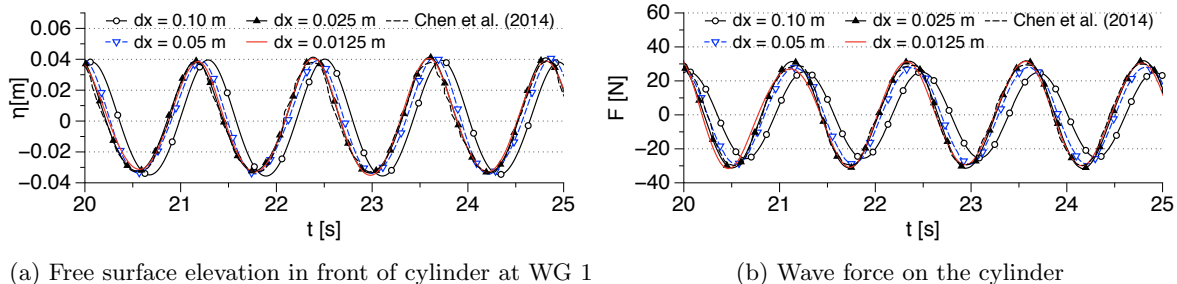


Figure 12: Grid convergence study for wave interaction with a vertical cylinder

cylinder is measured using four load cells placed on the top of the cylinder. The free surface elevation at various locations in the wave basin are measured. In the numerical wave tank, second-order Stokes waves of height $H = 0.07$ m, period $T = 1.22$ m are generated in a water depth $d = 0.505$ m. The relative wave steepness $ka = 0.104$ and the relative water depth $kd = 1.506$. The numerical wave tank is 20 m long, 3 m wide and 1 m high and a cylinder of diameter $D = 0.25$ m is placed at a distance of 7.52 m from the wave generation zone. A grid size of $dx = 0.025$ m is used, resulting in 3.456 million cells. No-slip boundary conditions are enforced on the lateral walls, the bottom of the wave tank and on the surface of the cylinder. The numerical setup is illustrated in Fig.(10).

The computed free surface elevation in front of the cylinder (WG 1) is compared to the experimental data in Fig.(11a) and a good agreement is seen. The amplitude spectrum of the computed free surface is compared to the amplitude spectrum of the free surface elevation measured in the experiments in Fig.(11b). It is seen that the free surface elevation has one major peak at $f_p = 0.79$ Hz, close to the fundamental frequency of the incident waves $f_0 = 0.82$ Hz. A small amplitude is seen for the first harmonic $f_1 = 1.64$ Hz, as the wave steepness is not very high. The calculated wave force on the cylinder is compared to the experimental measurements in Fig. (11c) and the amplitude spectra of the calculated and measured forces are compared in Fig.(11d). A good agreement is seen between the numerical and experimental results. The amplitude spectrum shows that the force at higher harmonics is negligible in this case.

A grid resolution study is carried out with $dx = 0.10$ m, 0.05 m and 0.0125 m and the computed wave force and free surface elevation converges to the experimental result at $dx = 0.025$ m as shown in Fig.(12). The selected grid resolution is found to be sufficient for the computation of the wave force on the cylinder and the free surface in the numerical wave tank.

4.4 Wave Propagation over a Submerged Bar

A well known benchmark is the submerged bar case by [2]. Here, monochromatic regular waves are generated in a rectangular wave flume of size $(L_x \times L_y \times L_z = 37.7 \text{ m} \times 0.8 \text{ m} \times 0.75 \text{ m})$. A trapezoidal submerged bar is placed 6 m downstream of the wave maker, see Fig. (13). Nine wave gages are placed along the wave flume. The incident wave height is $H = 0.02$ m with a wave period of $T = 2$ s, resulting in a wavelength $L = 3.73$ m. The incident relative wave steepness $ka = 0.0168$ and relative water depth $kd = 0.674$.

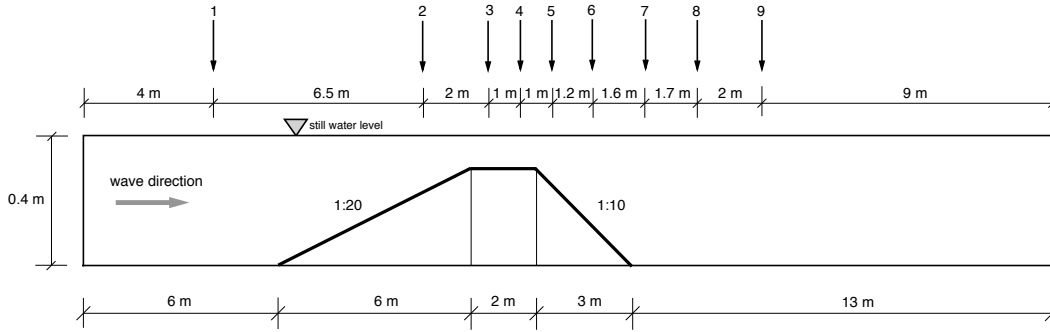


Figure 13: Submerged Bar setup with wave gage locations

In the numerical model, linear waves are generated in a relaxation zone of one wavelength. On the upslope of the bar, the waves shoal, yet breaking does not occur. After the crest of the bar, wave decomposition takes place and higher wave harmonics are formed. As a result, the free surface is typically very difficult to predict in the downslope and downstream region of the bar [3]. High-order numerical discretization schemes are needed in order to predict the correct dispersion characteristics and avoid wave crest damping and wave phase shifting. Thus, this case is well suited to test the accuracy of the proposed numerical wave tank. For the grid convergence study, two wave gages are selected: wave gage 4 on the crest of the submerged bar and wave gage 9 on the downstream side. Grids with $dx = (0.05 \text{ m}, 0.02 \text{ m}, 0.01 \text{ m}, 0.005 \text{ m})$ are tested.

Fig. (14j) reveals that the two finer meshes closely match the experimentally observed effect from shoaling. For the two coarser meshes, the shoaling is under predicted with lower free surface elevations in addition to slower moving waves. In Fig. (14k), it can be seen that the mesh with $dx = 0.005 \text{ m}$ can capture the transformed wave very well, both in amplitude and phase. The phase is also maintained for $dx = 0.01 \text{ m}$, while the wave crest is slightly reduced. For $dx = 0.025 \text{ m}$, the phase shift and the amplitude reduction is clearly visible, for $dx = 0.05 \text{ m}$ even more. As a result, the mesh with $dx = 0.005 \text{ m}$ is selected for the comparison with the experimental data. Wave gage 1 shows the input wave, with the wave crests and trough symmetric around the still water level, the typical characteristics for linear waves. Wave gage 2 shows the beginning of the shoaling on the sloping bed, but the waves maintain their sinusoidal shape. Gages 3 and 4 show the waves on the crest of the submerged bar. The loss of the sinusoidal shape indicates appearance of the secondary crests. This becomes more prominent on the downslope (gages 5 and 6) and on the downstream side of the submerged bar (gages 7-8).

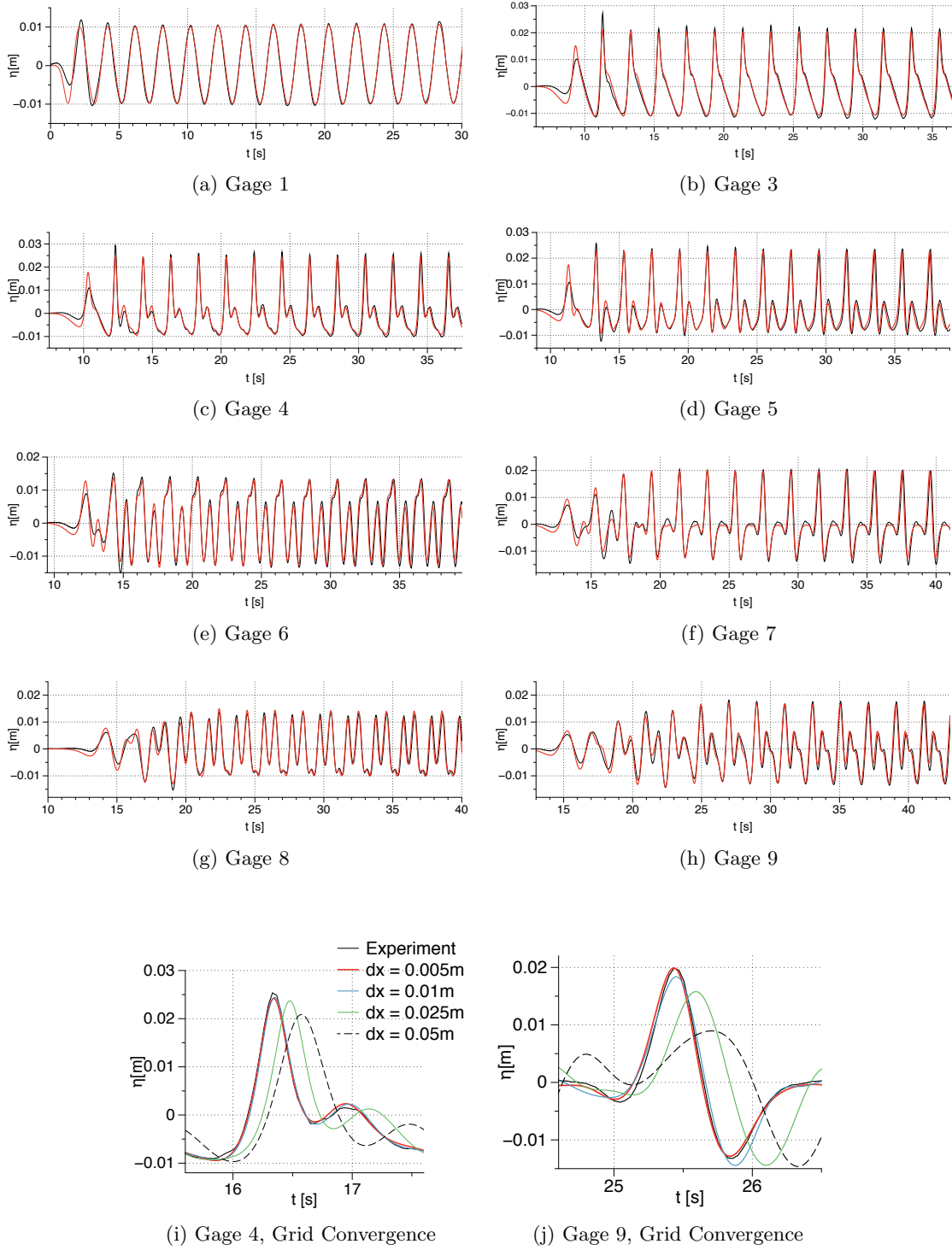


Figure 14: Wave transformation on a submerged bar, black lines are laboratory experiments, red lines are REEF3D.

For all gages, the free surface predicted by the numerical model closely follows the one recorded in the laboratory experiment. This demonstrates the capabilities of REEF3D due to the high-order spatial WENO and temporal TVD Runge-Kutta discretization in addition to the staggered grid arrangement. Also, the immersed boundary handles the irregular grid cells well on the slopes of the submerged bar.

4.5 Plunging Breaking Waves over a Sloping Bed

In the previous section, shoaling non-breaking waves were modeled. A more difficult situation arises, when the shoaling effect is so strong, that the steepened wave crest becomes unstable and breaks. A sloping seabed with a slope of 1/35 is chosen for the case study of wave breaking over a plane slope. The computational setup and wave parameters in the present case study are similar to the experimental conditions reported by [43]. The wave tank has a horizontal bed with the water depth of $d = 0.4$ m. A 4 m long stretch with a flat bottom is followed by the slope. The laboratory arrangements and the computational domain for the plunging breaker case are shown in Fig. (15). The origin of the horizontal and vertical coordinates is at the toe of the slope at the still water level. A fifth-order cnoidal wave theory developed by [14] is used to represent the incident wave with the height of $H = 0.128$ m and period of $T = 5.0$ s. The relative wave steepness and relative water depth of the incident wave are $ka = 0.041$ and $kd = 0.256$ respectively. A simulation length of 30 s is used to obtain a quasi-steady state for the mean wave quantities. Then the simulated values from the last five waves are used for the evaluation of the breaking point and breaking height.

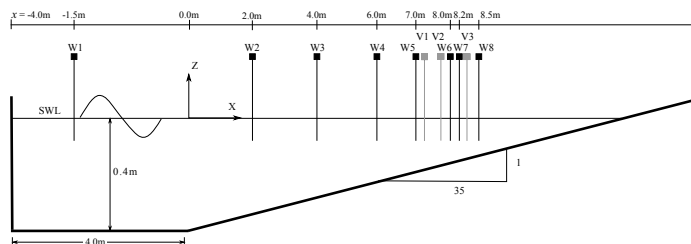


Figure 15: Computational set-up: W1-W8 are wave gauge locations and V1-V3 are velocity probe locations

The sensitivity of the computational results to the grid resolution is investigated with four different mesh sizes $dx = (0.025 \text{ m}, 0.01 \text{ m}, 0.005 \text{ m}, 0.0025 \text{ m})$. The simulated breaking location (x_b) and the breaker height (H_b) are compared with the measured data in Fig. (16). The simulated waves break later shoreward with slightly larger breaker height on coarser grids ($dx = 0.025 \text{ m}$ and $dx = 0.01 \text{ m}$) than in the experiments. Whereas on finer grids ($dx = 0.005 \text{ m}$ and $dx = 0.0025 \text{ m}$) waves break at almost the same location $x_b = 7.84 \text{ m}$ with the breaker height $H_b = 0.205 \text{ m}$ as in the experiments, where waves break at $x_b = 7.795 \text{ m}$ with $H_b = 0.196 \text{ m}$. The comparison of the experimental and numerical values indicates that the best comparison with experimental data occurs with the finer grids ($dx = 0.005 \text{ m}$ and $dx = 0.0025 \text{ m}$). The grid size $dx = 0.005 \text{ m}$ is selected for the computation since the simulated waves on this grid size yield good results with reasonable computational time and the difference between the $dx = 0.005 \text{ m}$ and $dx = 0.0025 \text{ m}$ is also insignificant. Compared to the previous section, a finer mesh is required. Here, the additional challenge arises not from

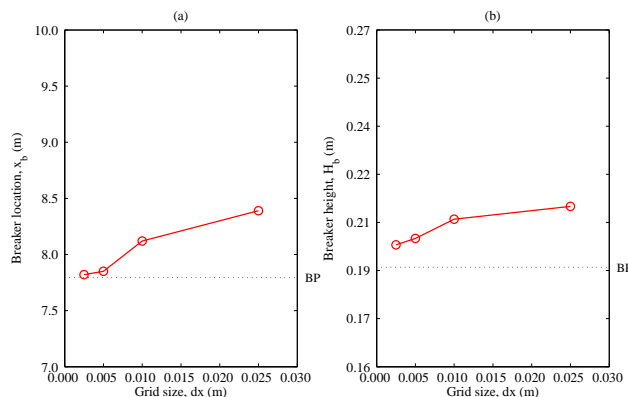


Figure 16: Grid sensitivity study on simulated results (a) breaker location (x_b) and (b) breaker height (H_b). The dotted line shows the breaking point observed in the experiments.

the wave shoaling, but from the breaking process. The breaking occurs at a much smaller scale, than the wave propagation itself. Also, wave breaking is a true two-phase flow problem, where complex interface deformations occur.

The simulated free surface elevations are compared with experimental data at different locations along the wave tank in order to assess the ability of the numerical model to simulate hydrodynamic processes from wave generation to the surf zone. The free surface elevations are computed at eight different locations (W1-W8): $x = -1.5$ m, 2.0 m, 4.0 m, 6.0 m, 7.0 m, 8.0 m, 8.2 m and 8.5 m from the toe of the slope (see Fig. (15)). Fig. (17) shows the comparison of the simulated free surface elevations with the experimental measurements [43] for the plunging breaker case. The free surface profile evolves continuously from a wide crest to a narrow and steep crest. The wave height increases due to shoaling, as the wave propagates over the slope. The wave crest becomes unstable and breaks at $x_b = 7.84$ m with a breaker height of $H_b = 0.205$ m. The numerical breaking condition is almost the same as measured in the experiments. It can be seen from Figs. 17 (f), (g) and (h), that the wave height diminishes after breaking as the wave approaches the shore. The simulated free surface profiles precisely represent the characteristics of the cnoidal waves in shallow water and display a good match with the experimental data.

The computed horizontal component of the fluid velocity at $x = 7.295$ m (before breaking), $x = 7.795$ m (during breaking) and $x = 8.345$ m (after breaking) are compared with the experimental data in Fig. (18) - Fig. (20). As can be seen from Fig. (18), in the region just prior to breaking, the variation of the horizontal velocity is almost constant with the water depth, which is consistent with the experimental observation by [43]. As the wave propagates further over the slope, the wave height increases due to shoaling. This leads to a rise in the potential energy in the region close to the wave crest. When the fluid particle velocity exceeds the wave speed, wave breaking occurs at $x = 7.84$ m, with the maximum velocity at the tip of the horizontal overturning jet followed by a small velocity gradient over the depth (Fig. (19)). At the point of jet impingement, the horizontal velocity increases as the distance from the free surface increases, as shown in Fig. (20). This is due to the penetration of the large scale water jet into the preceding wave surface. The present model predicts the horizontal velocity variation along the water depth accurately and the simulated results are in good agreement

with the experimental measurements.

The evolution of the wave breaking process with the velocity magnitude and velocity vector distribution is shown in Fig. (21). At the incipient breaking stage, the wave profile gets steeper and sharper and a portion of the wave crest attains the maximum fluid velocity. The total wave energy is focused near the wave crest and eventually wave breaking occurs. The portion of the wave crest with high velocity moves forward and evolves into an overturning plunging jet (Fig. (21a)). When the plunging jet impinges on the surface of the preceding wave (Fig. (21b)), a splash-up occurs as shown in Fig. (21c) and Fig. (21d). This creates a secondary wave followed by a pocket of air with different characteristics than the original wave. The rapid transition from a strong plunger vortex into small scale turbulence at the free surface takes place over a short distance. The simulated physical flow features of the plunging breaker during the wave breaking process such as wave profile evolution, the generation of the overturning water jet, the enclosed air pocket and the secondary wave, the splash-up phenomenon and the mixing of air and water in the surf zone are consistent with the experimental observation [43].

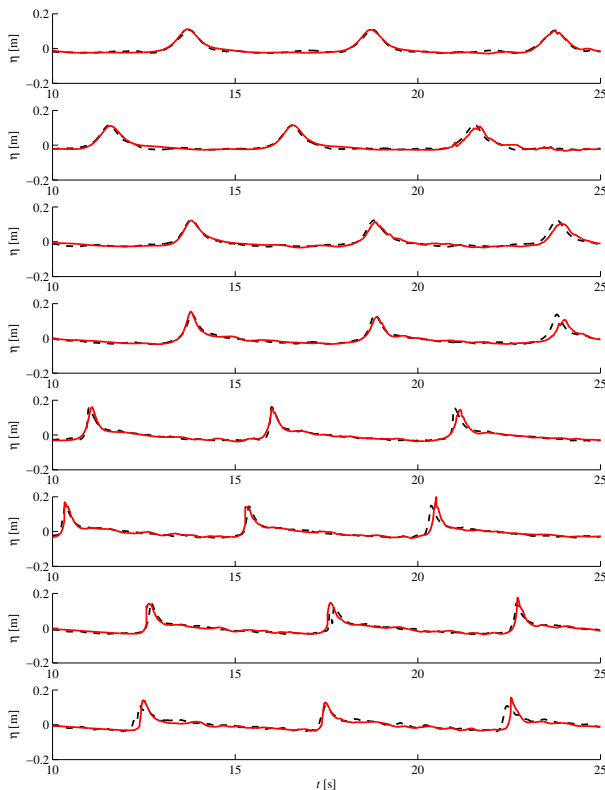


Figure 17: Comparison of simulated and measured water surface elevations for plunging breaker case at $x = -1.5$ m (a), 2.0 m (b), 4.0 m (c), 6.0 m (d), 7.0 m (e), 8.0 m (f), 8.2 m (g) and 8.5 m (h). Red lines: present numerical model; Black lines: experimental data by [43]

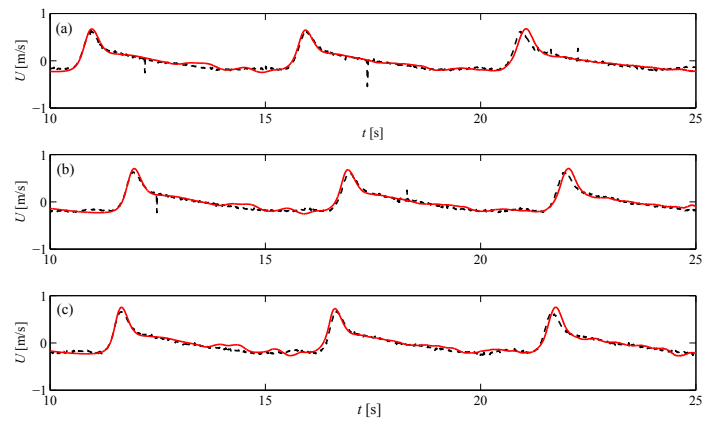


Figure 18: Comparison of simulated and measured horizontal velocities for plunging breaker case at $x=7.295$ m and $z=-0.05$ m (a), -0.10 m (b), and -0.15 m (c). Red lines: present numerical model; Black lines: experimental data by [43]

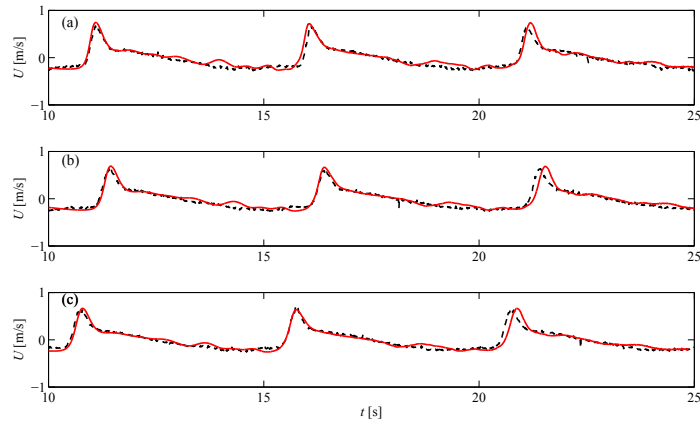


Figure 19: Comparison of simulated and measured horizontal velocities for plunging breaker case at $x=7.795$ m and $z=-0.05$ m (a), -0.10 m (b), and -0.145 m (c). Red lines: present numerical model; Black lines: experimental data by [43]

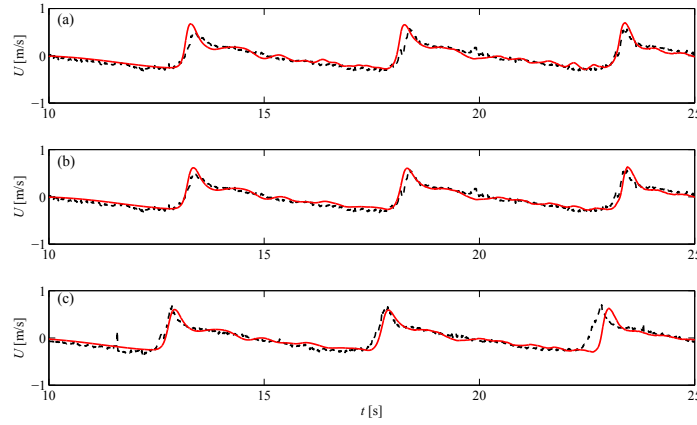


Figure 20: Comparison of simulated and measured horizontal velocities for plunging breaker case at $x=8.345$ m and $z=-0.05$ m (a), -0.10 m (b), and -0.13 m (c). Red lines: present numerical model; Red lines: experimental data by [43]

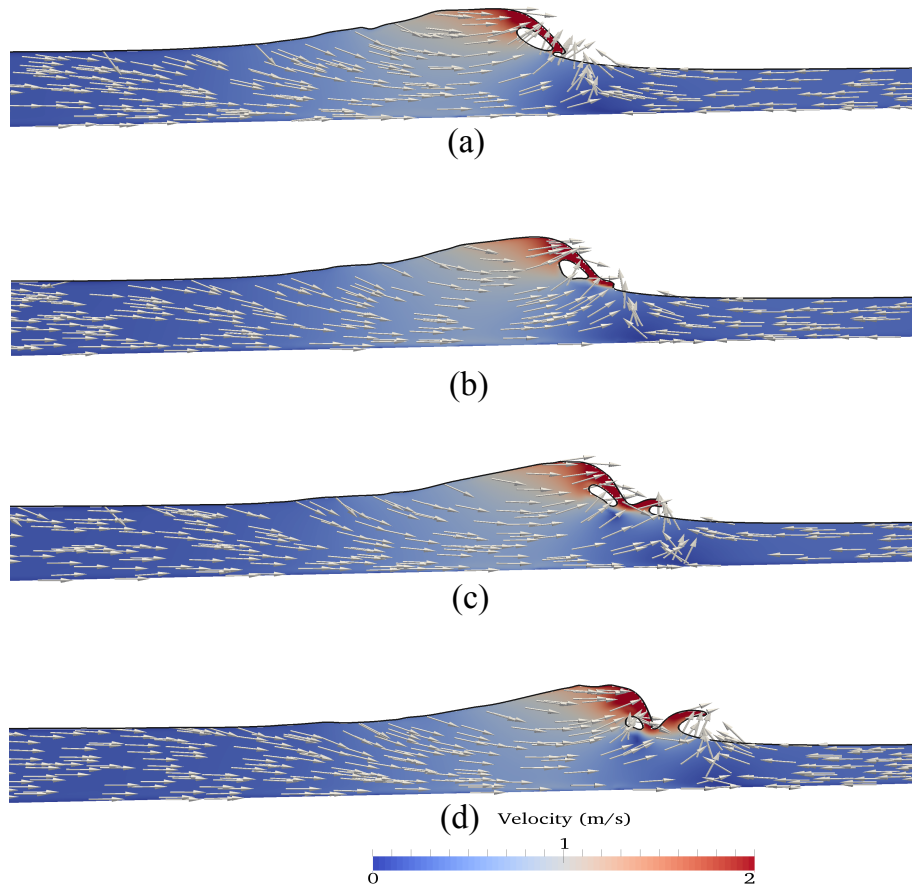


Figure 21: Snapshots of simulated wave profile during breaking process over a slope at $t = 10.90$ s (a), 10.95 s (b), 11.00 s (c) and 11.05 s (d)

5 Conclusions

The new numerical wave tank REEF3D has been presented. The incompressible Navier-Stokes equations are solved with RANS turbulence closure. In order to achieve stable and accurate wave propagation results, high-order numerical discretization schemes on a Cartesian mesh are selected. For the convection terms of the momentum equations, the fifth-order WENO scheme is chosen. Time-stepping is performed with the third-order TVD Runge-Kutta scheme. The pressure is solved on a staggered grid with the projection method, ensuring tight pressure-velocity coupling. Irregular boundaries are taken into account with an extension of an existing ghost cell immersed boundary method to three dimensions. The numerical model is fully parallelized based on the domain decomposition strategy and MPI (message passing interface). The free surface is modeled with the level set method. Special attention has been given to the evaluation of the density. It was found that density evaluation at the cell center leads to small-scale free surface oscillations, when periodic regular waves are simulated. The proposed density calculation scheme at the cell face showed a much improved free surface, comparing well against the theoretical wave profile. The waves are generated and absorbed with the relaxation method.

The performance of the proposed numerical wave tank has been tested with several benchmark applications. At first, grid and time step convergence tests have been performed for periodic regular waves. Next, the interaction of a solitary wave with a vertical structure was calculated. The comparison with experimental free surface measurements showed good agreement. Also, the coarse grids performed well for the solitary wave propagation problem. Further, the model was used to calculate non-breaking wave forces on a vertical cylinder. The model matched the experimental free surface, velocity and wave force data well, showing that the model also predicts the wave kinematics and wave dynamics very realistically. The challenging submerged bar case revealed that the numerical wave tank has the capability to accurately predict wave shoaling and the following wave transformation. In the last test, plunging breaking waves were modeled. The model compared favorably against the experimentally recorded free surface and velocity data. The plunging breaking waves were simulated in a realistic manner and all the stages of the breaking process were captured. The benchmark tests show that the new numerical wave tank REEF3D achieves the goal of accurately representing the physics of wave propagation and hydrodynamics, including the complex problem of wave breaking.

Acknowledgment

The authors would like to thank Prof. Iñigo J. Losada for providing the experimental data for the solitary wave interaction with a vertical structure. The authors would also like to thank Dr. James Kirby and Dr. Francis Ting for sharing the experimental data of the plunging breaking waves case. This study has been carried out under the OWCBW project (No. 217622/E20) and the authors are grateful to the grants provided by the Research Council of Norway. This study was supported in part with computational resources at the Norwegian University of Science and Technology (NTNU) provided by NOTUR, <http://www.notur.no>.

6 References

References

- [1] M. Alagan Chella, H. Bihs, D. Myrhaug, and M. Muskulus. Breaking characteristics and geometric properties of spilling breakers over slopes. *Coastal Engineering*, 95:4–19, 2015.
- [2] S. Beji and J. A. Battjes. Experimental investigation of wave propagation over a bar. *Coastal Engineering*, 19:151–162, 1993.
- [3] S. Beji and J. A. Battjes. Numerical simulation of nonlinear wave propagation over a bar. *Coastal Engineering*, 23:1–16, 1994.
- [4] P. A. Berthelsen and O. M. Faltinsen. A local directional ghost cell approach for incompressible viscous flow problems with irregular boundaries. *Journal of Computational Physics*, 227:4354–4397, 2008.
- [5] N. Booij, R. C. Ris, and L. H. Holthuijsen. A third-generation wave model for coastal regions, 1. model description and validation. *Journal of Geophysical Research*, 104:7649–7666, 1999.
- [6] A. Calderer, S. Kang, and F. Sotiropoulos. Level set immersed boundary method for coupled simulation of air/water interaction with complex floating structures. *Journal of Computational Physics*, 277:201–227, 2014.
- [7] L. F. Chen, J. Zang, A. J. Hillis, G. C. J. Morgan, and A. R. Plummer. Numerical investigation of wave–structure interaction using openfoam. *Ocean Engineering*, 88:91–109, 2014.
- [8] A. Chorin. Numerical solution of the Navier-Stokes equations. *Mathematics of Computation*, 22:745–762, 1968.
- [9] R. Croce, M. Griebel, and M. A. Schweitzer. Numerical simulation of bubble and droplet deformation by a level set approach with surface tension in three dimensions. *International Journal for Numerical Methods in Fluids*, 62:963–993, 2010.
- [10] D. G. Dommermuth and D. K. P. Yue. A high-order spectral method for the study of nonlinear gravity waves. *Journal of Fluid Mechanics*, 184:267–288, 1987.
- [11] D. G. Dommermuth, D. K. P. Yue, W. M. Lin, R. J. Rapp, E. S. Chan, and W. K. Melville. Deep-water plunging breakers : a comparison between potential theory and experiments. *Journal of Fluid Mechanics*, 189:434–442, 1988.
- [12] P. A. Durbin. Limiters and wall treatments in applied turbulence modeling. *Fluid Dynamics Research*, 41:1–18, 2009.
- [13] J. D. Fenton. A fifth-order Stokes theory for steady waves. *Journal of Waterway, Port, Coastal and Ocean Engineering*, 111(2):216–234, 1985.
- [14] J. D. Fenton. *The cnoidal theory of water waves*, chapter 2, pages 55–100. Developments in Offshore Engineering, Gulf, Houston. J. B. Herbich edition, 1999.

- [15] M. Griebel, T. Dornseifer, and T. Neunhoffer. *Numerical Simulation in Fluid Dynamics, a Practical Introduction*. SIAM, 1998.
- [16] S. T. Grilli, R. Subramanya, I. A. Svendsen, and J. Veeramony. Shoaling of solitary waves on plane beaches. *Journal Waterway Port Coastal and Ocean Engineering*, 120(6):609–628, 1994.
- [17] R. Grimshaw. The solitary wave in water of variable depth. part 2. *Journal of Fluid Mechanics*, 46:611–622, 1971.
- [18] P. Guyenne, S. T. Grilli, and b. v. p. y. Dias, F. Numerical modeling of fully nonlinear 3D overturning waves over arbitrary bottom.
- [19] A. Harten. High resolution schemes for hyperbolic conservation laws. *Journal of Computational Physics*, 49:357–393, 1983.
- [20] P. Higuera, L. J. Lara, and I. J. Losada. Realistic wave generation and active wave absorption for Navier-Stokes models application to OpenFOAM. *Coastal Engineering*, 71:102–118, 2013.
- [21] P. Higuera, L. J. Lara, and I. J. Losada. Simulating coastal engineering processes with OpenFOAM. *Coastal Engineering*, 71:119–134, 2013.
- [22] P. Higuera, L. J. Lara, and I. J. Losada. Three-dimensional interaction of waves and porous coastal structures using OpenFOAM. Part II: Application. *Coastal Engineering*, 83:259–270, 2014.
- [23] M. S. Hossain and W. Rodi. Mathematical modeling of vertical mixing in stratified channel flow. *2nd Symposium on Stratified Flows, Trondheim, Norway*, 1980.
- [24] N. G. Jacobsen, D. R. Fuhrman, and J. Fredsøe. A wave generation toolbox for the open-source CFD library: OpenFOAM. *International Journal for Numerical Methods in Fluids*, 70(9):1073–1088, 2012.
- [25] G. S. Jiang and D. Peng. Weighted ENO schemes for Hamilton Jacobi equations. *SIAM Journal of Scientific Computing*, 21:2126–2143, 2000.
- [26] G. S. Jiang and C. W. Shu. Efficient implementation of weighted ENO schemes. *Journal of Computational Physics*, 126:202–228, 1996.
- [27] J. T. Kirby and R. A. Dalrymple. A parabolic equation for the combined refraction-diffraction of Stokes waves by mildly varying topography. *Journal of Fluid Mechanics*, 136:453–466, 1983.
- [28] L. J. Lara, M. del Jesus, and I. J. Losada. Three-dimensional interaction of waves and porous coastal structures part II: Experimental validation. *Coastal Engineering*, 64:26–46, 2012.
- [29] P. A. Madsen, H. B. Bingham, and H. Liu. A new Boussinesq method for fully nonlinear waves from shallow to deep water. *Journal of Fluid Mechanics*, 462:1–30, 2002.

- [30] P. A. Madsen, R. Murray, and O. R. Sørensen. A new form of the Boussinesq equations with improved linear dispersion characteristics. *Coastal Engineering*, 15:371–388, 1991.
- [31] S. Mayer, A. Garapon, and L. S. Sørensen. A fractional step method for unsteady free surface flow with applications to non-linear wave dynamics. *International Journal for Numerical Methods in Fluids*, 28:293–315, 1998.
- [32] R. Mittal, H. Dong, M. Bozkurttas, F. M. Najjar, A. Vargas, and A. von Loebbecke. A versatile sharp interface immersed boundary method for incompressible flows with complex boundaries. *Journal of Computational Physics*, 227:4825–4852, 2008.
- [33] D. Naot and W. Rodi. Calculation of secondary currents in channel flow. *Journal of the Hydraulics Division, ASCE*, 108(8):948–968, 1982.
- [34] NOTUR. Notur - the Norwegian Metacenter for Computational Science. <http://www.notur.no>, 2015.
- [35] O. Nwogu. Alternative form of Boussinesq equations for nearshore wave propagation. *Journal of Waterways, Port, Coastal, and Ocean Engineering*, 119(6):618–638, 1993.
- [36] S. Osher and J. A. Sethian. Fronts propagating with curvature-dependent speed: Algorithms based on Hamilton-Jacobi formulations. *Journal of Computational Physics*, 79:12–49, 1988.
- [37] B. T. Paulsen, H. Bredmose, and H. Bingham. An efficient domain decomposition strategy for wave loads on surface piercing circular cylinders. *Coastal Engineering*, 86:57–76, 2014.
- [38] D. Peng, B. Merriman, S. Osher, H. Zhao, and M. Kang. A PDE-based fast local level set method. *Journal of Computational Physics*, 155:410–438, 1999.
- [39] W. E. Rogers, J. M. Kaihatu, L. Hsu, R. E. Jensen, J. D. Dykes, and K. T. Holland. Forecasting and hindcasting waves with the SWAN model in the Southern California Bight. *Coastal Engineering*, 54:1–15, 2007.
- [40] B. Seiffert, M. Hayatdavoodi, and R. C. Ertekin. Experiments and computations of solitary-wave forces on a coastal-bridge deck. Part I: Flat plate. *Coastal Engineering*, 88:194–209, 2014.
- [41] C. W. Shu and S. Osher. Efficient implementation of essentially non-oscillatory shock capturing schemes. *Journal of Computational Physics*, 77:439–471, 1988.
- [42] M. Sussman, P. Smereka, and S. Osher. A level set approach for computing solutions to incompressible two-phase flow. *Journal of Computational Physics*, 114:146–159, 1994.
- [43] F. C. K. Ting and J. T. Kirby. Dynamics of surf-zone turbulence in a strong plunging breaker. *Coastal Engineering*, 24:177–204, 1995.
- [44] Y. H. Tseng and J. H. Ferziger. A ghost-cell immersed boundary method for flow in complex geometry. *Journal of Computational Physics*, 192:593–623, 2003.

- [45] H. van der Vorst. BiCGStab: A fast and smoothly converging variant of Bi-CG for the solution of nonsymmetric linear systems. *SIAM Journal of Scientific Computing*, 13:631–644, 1992.
- [46] B. van Leer. Towards the ultimate conservative difference scheme V. A second order sequel to Godunovs method. *Journal of Computational Physics*, 32:101–136, 1979.
- [47] Z. Wang, J. Yang, and F. Stern. A coupled level set and volume-of-fluid method for sharp interface simulation of plunging breaking waves. *International Journal of Multiphase Flow*, 35:227–246, 2009.
- [48] H. G. Weller. A new approach to VOF-based interface capturing methods for incompressible and compressible flow. *Technical Report. OpenFOAM*, 2008.
- [49] R. Wemmenhove. *Numerical Simulation of Two-Phase Flow in Offshore Environments*. PhD thesis, Faculty of Mathematics and Natural Sciences, University of Groningen, 2008.
- [50] D. C. Wilcox. *Turbulence Modeling for CFD*. DCW Industries Inc., La Canada, California., 1994.
- [51] G. X. Wu and R. E. Taylor. Finite element analysis of two-dimensional non-linear transient water waves. *Applied Ocean Research*, 16(6):363–372, 1994.
- [52] F. Xu, W. Perrie, B. Toulany, and P. C. Smith. Wind-generated waves in Hurricane Juan. *Ocean Modeling*, 16:188–205, 2007.
- [53] J. Yang and F. Stern. Sharp interface immersed-boundary/level-set method for wave-body interactions. *Journal of Computational Physics*, 228:6590–6616, 2009.
- [54] J. Yang and F. Stern. Robust and efficient setup procedure for complex triangulations in immersed boundary simulations. *Journal of Fluids Engineering*, 135(10):101107.1–101107.11, 2014.
- [55] W. Yue, C.-L. Lin, and V. C. Patel. Numerical simulation of unsteady multidimensional free surface motions by level set method. *International Journal for Numerical Methods in Fluids*, 42:853–884, 2003.